nature nanotechnology

SUPPLEMENTARY INFORMATION

https://doi.org/10.1038/s41565-018-0227-7

In the format provided by the authors and unedited.

Tunable thermal transport and reversible thermal conductivity switching in topologically networked bio-inspired materials

John A. Tomko[1,10], Abdon Pena-Francesch[2,3,10], Huihun Jung[2,3], Madhusudan Tyagi[4,5], Benjamin D. Allen[6,7], Melik C. Demirel[2,3,7]* and Patrick E. Hopkins[1,8,9]*

[1]Department of Materials Science and Engineering, University of Virginia, Charlottesville, VA, USA. [2]Center for Research on Advanced Fiber Technologies (CRAFT), Materials Research Institute, Pennsylvania State University, University Park , PA, USA. [3]Department of Engineering Science and Mechanics, Pennsylvania State University, State College, PA, USA. [4]NIST Center for Neutron Research, Gaithersburg, MD, USA. [5]Department of Materials Science and Engineering, University of Maryland, College Park, MD, USA. [6]Department of Biochemistry and Molecular Biology, Pennsylvania State University, University Park, PA, USA. [7]Huck Institutes of the Life Sciences, Pennsylvania State University, University Park, PA, USA. [8]Department of Mechanical and Aerospace Engineering, University of Virginia, Charlottesville, VA, USA. [9]Department of Physics, University of Virginia, Charlottesville, VA, USA. [10]These authors contributed equally: John A. Tomko, Abdon Pena-Francesch. *e-mail: MDemirel@engr.psu.edu; phopkins@virginia.edu

Table I. Data of thermal conductivity switches from Figure 4c in Manuscript

Material	**Switching Temperature (K)**	**Thermal Conductivity Switch Ratio ($\kappa_{max}/\kappa_{min}$)**	**Switching Mechanism**
TR-n4	295	1.65±0.25	Hydration
TR-n7	295	2.74±0.30	Hydration
TR-n11	295	4.10±0.46	Hydration
TR-n25	295	3.92±0.31	Hydration
TR-n∞	295	4.54	Hydration
H_2O[1]	273	2.66	Phase change (S/L)
Li_xCoO[22]	295	1.45	Electrochemical lithiation
C_{70}[3]	298	1.45	Applied pressure
PZT[4]	298	1.11	Ferroelectric domain scattering (electric field)
B nanoribbon[5,6]	300	1.61	Wetting
SWCNT/n-$C_{18}H_{38}$[7]	303	2.5	Phase change (S/L)
Ga[8–10]	303	1.57	Phase change (S/L)
PEG4000[11]	313.15	1.42	Phase change (S/L)
K[9,10]	337	1.80	Phase change (S/L)
VO_2[12]	340	1.41	Metal-insulator transition (S/S)
RM257[13]	353	1.55	Molecular reorientation (magnetic field)

Time-domain thermoreflectance (TDTR)

In this work, we use a two-color setup, where a train of 80 MHz, 90 fs, 800 nm laser pulses emanates from a Ti:Sapphire oscillator (Spectra Physics Tsunami) and is split into a pump and probe path. The pump pulses are electro-optically modulated at a frequency of 8.8 MHz and then frequency-doubled to 400 nm, allowing us to perform our TDTR measurements with both Al and Au transducers (due to increase absorption in Au at 400 nm). The probe pulse remains at 800 nm and is mechanically delayed to create a temporal delay between the pump and probe. The thermoreflectance of the probe is measured via lock-in detection as a function of the pump-probe delay time to obtain the thermal decay from the metal transducer into the surrounding films. Note, we have measured the thermal conductivity of the protein films under varying experimental conditions, namely with different objectives and power densities during the TDTR measurements. The most repeated experimental conditions were the use of a 10X objective, leading to a pump diameter of ~19 μm and a probe diameter of ~9 μm with typically less than a 15 mW pump power while modulating the pump pulses at 8.8 MHz. The probe power was ~5 mW. These laser powers were specifically aimed towards avoiding denaturation of the protein film due to large local temperature rises during the TDTR scan while still obtaining a large enough out-of-phase signal for reliable data.

To ensure the metal film is optically specular, we electron-beam evaporate either the Al or Au film on amorphous SiO_2 substrates and then solvent-cast the TR film on the opposing side of the deposited 80 nm metal transducer; the protein films are dried overnight and then washed with DI water.

We perform the TDTR measurement through the transparent substrate in a "probe-up" geometry; a photograph of this upright schematic is shown in Fig.S1 as well as depicted in the manuscript in Fig.1a. The experimentally measured decay curve is fit to a bidirectional thermal model. An example of the fit is shown in Fig. S2 for TR-n25 in both ambient and hydrated conditions. For the hydrated measurements, we simply apply 500 μL of DI water on top of the TR film in the probed region; to return to 'ambient' conditions, this drop is pipetted off the surface. We find that the thermal conductivity switches on the order of typical liquid diffusion times (i.e., on the order of seconds); we are able to repeatedly measure this change in thermal conductivity via TDTR with no experimental waiting time between scans. Note, we find an asymmetry in the "switch on" time upon hydration) and "switch off" time when the water is removed; this phenomena is discussed in detail in the following section of the Supplementary Information.

As the best-fit value in this model relies on the dependence of knowing the thermal properties of the SiO_2 substrate and 80 nm metal film, we measure the film/substrate system prior to deposition of the proteinaceous films. Our thermal model accounts for the following values: we experimentally measure κ_{SiO2} = 1.35 W m^{-1} K^{-1}, insure the film thickness is 80 nm via profilometry and picosecond acoustic measurements, and κ_{Al} = 130 W m^{-1} K^{-1} based on electrical resistivity and TDTR measurements. The heat capacity of the substrate and film are based on literature values of 1.66 and 2.42 MJ m^{-3} K^{-1} respectively. Furthermore, due to the three-layer system and relatively low thermal conductivity of the TR films, TDTR is equally sensitive to both the heat capacity and thermal conductivity of the material (i.e., the thermal model can only fit for thermal diffusivity, $\frac{\kappa}{C_v}$, in this region. As we measure the volumetric heat capacity of our protein films in both ambient and hydrated conditions via DSC, as discussed in a later section, we are able to fit for solely the thermal conductivity of the TR film. The values used for our TDTR analysis are tabulated in Table II.

Table II. Measured material parameters for TR films and comparison to R.T. thermal switches

Sample	TR-n4	TR-n7	TR-n11	TR-n25
n (repeat units)	4	7	11	25
M.W. (kDa)	15	25	42	86
$C_{v,\text{ambient}}$ (MJ m^{-3} K^{-1})	1.76	1.71	1.73	1.72
κ_{ambient} (W m^{-1} K^{-1})	0.35 ± 0.09	0.34 ± 0.11	0.27 ± 0.10	0.33 ± 0.10
$C_{v,\text{hydrated}}$ (MJ m^{-3} K^{-1})	2.47	2.60	2.77	2.82
κ_{hydrated} (W m^{-1} K^{-1})	0.58 ± 0.09	0.93 ± 0.10	1.12 ± 0.13	1.30 ± 0.10
Ratio ($\kappa_{max}/\kappa_{min}$)	1.65 ± 0.26	2.74 ± 0.30	4.10 ± 0.46	3.92 ± 0.31
Material	**Switching Temperature (K)**	**Thermal Conductivity Switch Ratio ($\kappa_{max}/\kappa_{min}$)**	**Switching Mechanism**	
H_2O[1]	273	2.66	Phase change (S/L)	
Li_xCoO[22]	295	1.45	Electrochemical lithiation	
C_{70}[3]	298	1.45	Applied pressure	
PZT[4]	298	1.11	Ferroelectric domain scattering (electric field)	
B nanoribbon[5,6]	300	1.61	Wetting	
SWCNT/n-$C_{18}H_{38}$[7]	303	2.5	Phase change (S/L)	
Ga[8–10]	303	1.57	Phase change (S/L)	
PEG4000[11]	313.15	1.42	Phase change (S/L)	
K[9,10]	337	1.80	Phase change (S/L)	

VO_2[12]	340	1.41	Metal-insulator transition (S/S)
RM257[13]	353	1.55	Molecular reorientation (magnetic field)

To confirm the sensitivity and uncertainty associated with our bidirectional model to the thermal conductivities of materials on the order of our TR films, we use identical 80 nm Al films on SiO_2 substrates as were used for the biopolymer films, and instead spin-coat 200 nm PMMA, Poly(methyl-methacrylate), films on the Al film (PMMA/Al/SiO_2). Additionally, we use a separate film and add water to the top of the Al film (water/Al/SiO_2). In both cases, we use the same parameters and model as used for the biopolymer film measurements. In accounting for the propagation of error in values used for our thermal model, as discussed below, we measure the thermal conductivity of water at room temperature to be 0.59 ± 0.1 W m^{-1} K^{-1} and the thermal conductivity of PMMA to be 0.18 ± 0.07 W m^{-1} K^{-1}; these values are in excellent agreement with literature values for the two media.

Although we 'reference' the supporting metal transducer and underlying SiO_2 substrate, as discussed above, the propagation of error within these values leads to increased uncertainty in the measured thermal conductivity of our TR films. To accurately determine the true uncertainty in our TDTR measurements, we consider the mean square deviation of our bi-directional, three-layer thermal model to the experimental TDTR data obtained for the various TR films; this contour analysis uncertainty calculation is discussed in detail in previous references[14,15]. To summarize, the contour displays the normalized residual, or the model's mean square deviation, relative to the experimentally measured thermal decay curve; an increase in the normalized residual is equivalent to a poor fit to the data. For the bi-directional thermal model, with the thermal effusivities investigated in this work, the most sensitive parameter is the thickness of the metal transducer. Thus, in considering the maximum possible uncertainty in the values of best fit for our thermal conductivity measurements of the TR films, we extend this sensitivity analysis to 5% error in film thickness, as shown in Fig. S3; we find that our fits to the experimental data lie within the inner most contour, in dark blue. Given such, this contour denotes the uncertainty in thermal conductivity for a 5% uncertainty in film thickness (the thermal model's most sensitive parameter). Additionally, repeating these contours for various thermophysical parameters in our model, such as thermal conductivity of the SiO2 substrate leads to nearly identical contour plots (i.e., the model is not highly sensitive to this parameter). We plot the inner-most contour for TR-n25 as an example with the reference value of the SiO_2 substrate (1.35 W m^{-1} K^{-1}) and ± 10% of this value in Fig. S4.

To rule out potential metal/protein interactions that may be leading to the measured change in thermal conductivity upon hydration, we repeat the measurements using Au transducers of the same thickness. The results are shown in Fig. S5. As seen, the two are in good agreement and provide similar switching values between the two states.

To further reinforce the accuracy of the thermal conductivity values reported in this work, it should be noted that a minimum of four samples per TR film were measured; we conducted no

less than 40 TDTR scans on each of these samples (e.g., the thermal switch measurement for TR-n25 was performed over 200 times alone). Additionally, the majority of these measurements are conducted on various points throughout the sample to account for any inhomogeneity in either the metal transducer or TR film. The standard deviation of these measurements is accounted for in our reported error.

Switch times and water content

In the data reported in this work, we conduct TDTR scan once the samples have achieved their "fully on" (hydrated) or "fully off" (ambient) state. Note, throughout this work, we define ambient as being the TR protein in an unsaturated, ambient environment; for our TDTR measurements at the University of Virginia, we measure the relative humidity of our laboratory to be between 28-35%. Conversely, the hydrated measurements are performed on a position of the TR protein film that is fully submerged in an aqueous environment, as described in the previous section. As a single TDTR scan takes approximately two minutes, we cannot conduct full TDTR scans during the transition from ambient to hydrated to gain insight into the time scale associated with the switching of thermal conductivity in the TR films. However, to quantify the order of magnitude of this thermal conductivity switching time, we instead use the TDTR signal as a relative monitor of the temperature change by monitoring the TDTR signal at a single pump-probe delay time as a function of lab time while manually pipetting of water on and off of the sample to repeatedly hydrate and dry the sample. We have used this this approach of "staring" at the TDTR signal in to observe real time changes in thermal conductivity in various samples previously[4,16]. We note that in our current case, this procedure does indeed produce variabilities in the absolute switching times due to inadvertent changes in the manual application and removal of the water, along with sample to sample variabilities in film thickness which will change liquid diffusion times through the materials. Thus, while these measurements prevent us from absolutely quantifying the intrinsic switching times of these materials with high precision, this does allow for order of magnitude quantification of the switching times. While we discuss this procedure in more detail below, we note that all reported thermal conductivity values in this work are determined when the system has equilibrated in either the full hydrated or fully ambient states, as previously mentioned. In other words, the full TDTR scans that result in the thermal conductivity data presented in the main manuscript are only performed when there is no temporal fluctuation in the measured lock-in signal.

To give insight into the switching time, we fix our pump-probe delay time to 500 picoseconds and measure the lock-in signal as a function of lab time. From there, we repeatedly hydrate and dry the sample, via manual pipetting of water, over the course of minutes. To convert the measured signal to thermal conductivity as a function of time, we normalize the signal to the measured ratio from TDTR scans for the ambient and hydrated states at 500 picoseconds. The results for the TR films are shown in Fig. 4a of the primary manuscript for TR-n25. Upon hydration, the change in thermal conductivity is on the order of seconds.

Note: the reported thermal conductivity values in this work are when the system has equilibrated in either the ambient or hydrated state. In other words, the TDTR scans are only performed when there is no fluctuation in the magnitude of the lock-in signal.

In an attempt to quantify the role of varying water concentrations associated with this switch, we performed our TDTR measurements on TR-n11 and -n25 up to 92% relative humidity using a custom-built chamber (see Fig.S1). Although the chamber and sample have excessive

condensation, as shown in Fig.S6b, where water droplets similar to those used for our initial switching experiments are visible on every surface in the chamber including the inset which shows our TR-n11 sample, our probed region remains dry due to localized laser heating. This finding is in conceptual agreement with the rapid switch time found when our sample is dried through manual pipetting of a water droplet; our TDTR measurement leads to a steady-state temperature rise from laser heating, which causes rapid local evaporation from the probed region. In the case of humidity/concentration measurements, this local heating disallows for condensation in the measured area.

Time-domain Brillouin scattering

We measure the group velocity of coherent acoustic phonons through pump-probe Brillouin scattering measurements using a two-tint version of our TDTR apparatus. In pump-probe reflection measurements, such as TDTR, the initial pump pulse creates a heating event in the transducer; the energy imparted from the laser pulse paired with this temperature rise leads to the formation of coherent acoustic wave within the surrounding media. As a coherent acoustic wave traverses this media, in our case the TR films, the probe beam is partially reflected due to the change in refractive index associated with the pressure gradient; the transmitted portion of the beam continues towards the metal transducer and undergoes thermo-reflection as with a traditional TDTR measurement. As described in previous works[17–19], these two reflected beams will interfere and lead to periodic oscillations in the time-dependent reflectance signal. The intensity of this time-independent signal can be described via

$$I(t,T) = A * \exp(-\Gamma t) * \cos\left(\left(\frac{2\pi}{T}\right)t - \delta\right) - B * \exp\left(-\frac{t}{\tau}\right) \quad \text{(S1)}$$

where A, B, and δ are essentially scale factors, Γ is the damping of the acoustic wave-front due to energy dissipation, T is the period of the pressure front, and the second term, $\exp(-t/\tau)$ accounts for the thermal decay associated with traditional thermo=reflectance at the metal transducer. When the probe beam is at normal incidence, the frequency, f, (i.e., the inverse of the period, T) can be related to the sound speed of the partially transparent material via

$$f = \frac{2rv}{\lambda} \quad \text{(S2)}$$

where r is the index of refraction, λ is the wavelength of the probe beam, and v is the velocity of this coherent wave-front. In the case of our TR films, r has been determined in our previous work[20] and our probe beam is 800 nm.

Note, we utilize a two-tint pump-probe apparatus (i.e., the pump beam is also 800 nm) for these measurements to avoid damage of the TR film; as described in our previous work[21], direct interaction between the protein film and the 400 nm pump used in our TDTR measurements leads to gradual degradation of the film. In the hydrated measurements, the sample is fully submerged beneath 3 mm of DI water; the signal-to-noise ratio in the hydrated case is greatly reduced compared to that of the films in ambient conditions. Nonetheless, well-defined peaks remain visible, showing clear reduction in sound velocities compared to the ambient samples. The results from our measurements/calculations are provided in Table III of the Supplementary Information.

Table III. TDBS measurements

Sample	TR15 (-n4)	T42 (n11)
Ambient Velocity (m/s)	2374±45	1768±200
Hydrated Velocity (m/s)	2088±291	1805±291
Ambient C_v, (MJ m^{-3} K^{-1})	1.76	1.73
Hydrated C_v, (MJ m^{-3} K^{-1})	2.47	2.77
Ambient MSD ($Å^2$)	0.55	0.55
Hydrated MSD ($Å^2$)	1.5	1.5
Calculated Switching Ratio	~3.70	~4.90

Protein structure

As shown in Figure 1b of the primary manuscript, the proteins are composed of *β*-sheet crystallites, which are rich in alanine, and are 2 x 2.5 nm in size, and are connected by ~3 nm amorphous strands, which are rich in glycine.

As X-ray diffraction techniques are not optimal to investigate the structure and conformation of proteins, since they only provide information about the ordered domains (*β*-sheets) but not about the disordered strands, we have performed structural analysis of the ambient and hydrated proteins by Fourier transform infrared (FTIR) spectroscopy (Figure S8). Amide I band (1600-1700 cm^{-1}) corresponds to carbonyl stretching vibration, and thus contains information about the protein backbone confirmation and overall secondary structure. The amide I band of ambient and hydrated proteins is similar, showing that there are not significant structural changes upon hydration. For further analysis and determination of the crystallinity (i.e., *β*-sheet content), we analyzed the secondary structure via Fourier self-deconvolution (FSD) of the amide I band and corresponding fitting of individual Gaussian functions (Figure S9)[22]. The secondary structure content of ambient and hydrated films are similar (within error of each other), with a *β*-sheet content of 54%, and amorphous strands adopting 20% random coil, 7% *α*-helix, and 18% turn conformations.

Rheology

SRT proteins were compressed in PDMS molds (hydrated, 70 °C) into disk shaped samples of 2 mm in diameter and 1 mm in height. Measurements were performed in a Rheometric Scientific ARES rheometer with 3 mm diameter parallel plate geometry with a 10 mL liquid reservoir in the bottom plate. Samples were adhered to the plates using Click Bond CB200 adhesive (2 hour curing time at room temperature, with modulus in the GPa range). Liquid was fed into the reservoir with a peristaltic pump (Ultra Low Flow Mini-pump model 3384, Control Company) with

a flow rate of 0.4 mL/min to compensate for evaporation, and the system was equilibrated at 70 °C for 90 minutes.

Dynamic mechanical analysis (DMA)

DMA was performed in a TA 800Q DMA instrument, which has a force range of 10^{-4} to 18 N, force resolution of 10^{-5} N, strain resolution of 1 nm, and a frequency range of 0.01 to 200 Hz. DMA was used for small deformation analysis (oscillatory strain and strain ramp) in order to measure the glassy mechanics and glass transition of SRT proteins. Film-tension and submersion-tension clamps were used for ambient and hydrated (saturation) measurements respectively. Sample dimensions were 15 mm × 2.5 mm × 0.2 mm for the ambient test and 25 mm × 2.5 mm × 0.2 mm for the hydrated test. Oscillatory temperature sweep experiments were performed at 1 Hz, with amplitude of 2 μm and a rate of 2 °C per minute. Stress-strain experiments were performed with a strain rate of 1% per minute and a preload of 0.01 N.

Temperature modulated differential scanning calorimetry (TMDSC)

TA Instruments Q200 DSC was used for the glass transition measurements of SRT proteins. The instrument was calibrated for specific heat C_p measurements using T_{zero} aluminum pans and sapphire standard materials, including cell resistance and capacitance, cell constant and temperature calibration. SRT samples were annealed on a hot plate at 100 °C for 30 minutes in order to remove water before the experiment. Hydrated proteins were immersed in DI water for 1 hour, excess water was removed, and samples were sealed in hermetic pans. Samples were heated at 2 °C/min from 25 °C to 210 °C (beginning of thermal degradation) with a modulation period of 60 seconds and a temperature amplitude of 0.318 °C. Hydrated samples were run from 5 °C to 60 °C with the same rate, modulation period, and amplitude parameters. The glass transition was analyzed from the reversing specific heat capacity C_p data. The increase in heat capacity ΔC_p is calculated as the difference between the glassy and rubbery tangent lines: $C_p(T)^{rubbery} = C_p(T)^{glassy} + \Delta C_p$. The glass transition temperature is calculated as the step change midpoint: $C_p(T_g) = C_p(T_g)^{glassy} + \Delta C_p/2$. $C_p(T)^{glassy}$ and $C_p(T)^{rubbery}$ are the extrapolation of the tangent to the specific reversing C_p below and above the glass transition respectively. The measured heat capacity values in both the ambient and hydrated states are listed in Table II.

It should be noted that the aforementioned aluminum hermitic pans allow for the use of liquids and prevent evaporation as the sample is heated. This is not a problem when measuring TR proteins in ambient conditions, since the proteins are previously annealed to remove any moisture. Although they can be heated up to 200 °C, they thermally degrade as other structural proteins[23,24]. However, high temperature characterization and thermal degradation are not the focus of this work and are not discussed in this manuscript. On the other hand, absorbed water in hydrated proteins does suppose a problem for high temperature calorimetry. Although the hermetic pans prevent the evaporation of water, water vapor pressure buildup at higher temperatures can breach the sealed pan. Besides changing the hydration conditions of the sample of interest, a water vapor breach will generate a false endotherm artifact due to the evaporation, and can potentially damage the calorimeter cell. For these reasons, TMDSC measurements of hydrated protein samples were performed from 5 to 50 °C only, and they were not cycled to prevent any water vapor pressure buildup inside the hermetic cells. The measurements were repeated for each sample to ensure reproducibility and signal overlap (two measurements of each are plotted in Figure S10).

Neutron Scattering

Quasielastic neutron scattering experiments were performed at NIST Center for Neutron Research (NCNR), Gaithersburg MD. Experiments on ambient SRT proteins were performed on the high-flux backscattering spectrometer (HFBS)[25], with energy resolution of 1 μeV, dynamic range of ±15 μeV and Q-range of 0.25 $A^{\circ\,-1}$ - 1.8 $A^{\circ\,-1}$, at 295 K. The resolution function was measured at 4 K (signal is completely elastic). Quasielastic experiments on D_2O-hydrated SRT-TR polypeptides were performed on the disk chopper time-of-flight spectrometer (DCS)[26], with energy resolution of 64 μeV (wavelength λ = 6 Å), dynamic range of ±0.5 meV and Q-range of 0.1 $Å^{-1}$ - 2 $Å^{-1}$, at 295 K. Vanadium was used as the resolution function in DCS measurements.

† MDemirel@engr.psu.edu
‡phopkins@virginia.edu

1. Slack, G. A. Thermal conductivity of ice. *Physical Review B* **22,** 3065-3071 (1980).
2. Cho, J., Losego, M. D., Zhang, H. G., Kim, H., Zuo, J., Petrov, I., Cahill, D. G., & Braun, P. V. Electrochemically tunable thermal conductivity of lithium cobalt oxide. *Nature Communications* **5,** 4035 (2014).
3. Soldatov, A. & Sundqvist, B. Molecular rotation in C70 at high pressures: A thermal conductivity study. *Journal of Physics and Chemistry of Solids* **57,** 1371–1375 (1996).
4. Ihlefeld, J. F., Foley, B. M., Scrymgeour, D. A., Michael, J. R., Mckenzie, B. B., Medlin, D. L., Wallace, M., Trolier-Mckinstry, S., & Hopkins, P. E. Room-Temperature Voltage Tunable Phonon Thermal Conductivity via Reconfigurable Interfaces in Ferroelectric Thin Films. *Nano Letters* **15,** 1791-1795 (2015).
5. Kim, K. & Kaviany, M. Thermal conductivity switch: Optimal semiconductor/metal melting transition. *Physical Review B* **94,** 155203 (2016).
6. Yang, J., Yang, Y., Waltermire, S. W., Wu, X., Zhang, H., Gutu, T., Jiang, Y., Chen, Y., Zinn, A. A., Prasher, R., Xu, T. T., & Li, D. Enhanced and switchable nanoscale thermal conduction due to van der Waals interfaces. *Nature Nanotechnology* **7,** 91-95 (2012).
7. Harish, S., Ishikawa, K., Chiashi, S., Shiomi, J., & Maruyama, S. Anomalous thermal conduction characteristics of phase change composites with single-walled carbon nanotube inclusions. *Journal of Physical Chemistry C* **117,** 15409–15413 (2013).
8. Samsonov, G. V. *Handbook of the Physicochemical Properties of the Elements*. Springer Science & Business Media (2012).
9. Ho, C. Y., Powell, R. W., & Liley, P. E. Thermal Conductivity of the Elements. *Journal of Physical and Chemical Reference Data* **1,** 279-421 (1972).
10. Dyos, G. T., & Farrell, T. *Electrical Resistivity Handbook*. IET (1992).
11. Chen, R., Cui, Y., Tian, H., Yao, R., Liu, Z., Shu, Y., Li, C., Yang, Y., Ren, T., Zhang, G., & Zou, R. Controllable Thermal Rectification Realized in Binary Phase Change Composites. *Scientific Reports* **5,** 8884 (2015).
12. Oh, D. W., Ko, C., Ramanathan, S., & Cahill, D. G. Thermal conductivity and dynamic heat capacity across the metal-insulator transition in thin film VO2. *Applied Physics Letters* **96,** 151906 (2010).

13. Shin, J., Kang, M., Tsai, T., Leal, C., Braun, P. V., & Cahill, D. G. Thermally Functional Liquid Crystal Networks by Magnetic Field Driven Molecular Orientation. *ACS Macro Letters* **5,** 955-960 (2016).
14. Feser, J. P., & Cahill, D. G. Probing anisotropic heat transport using time-domain thermoreflectance with offset laser spots. *Review of Scientific Instruments* **83,** 104901 (2014).
15. Giri, A., Niemela, J. P., Tynell, T., Gaskins, J. T., Donovan, B. F., Karppinen, M., & Hopkins, P. E. Heat-transport mechanisms in molecular building blocks of inorganic/organic hybrid superlattices. *Physical Review B* **93,** 115310 (2016).
16. Donovan, B. F., Tomko, J. A., Giri, A., Olson, D. H., Braun, J. L., Gaskins, J. T., & Hopkins, P. E. Localized thin film damage sourced and monitored via pump-probe modulated thermoreflectance. *Review of Scientific Instruments* **88,** 054903 (2017).
17. Ma, W., Miao, T., Zhang, X., Kohno, M., & Takata, Y. Comprehensive Study of Thermal Transport and Coherent Acoustic-Phonon Wave Propagation in Thin Metal Film-Substrate by Applying Picosecond Laser Pump–Probe Method. *The Journal of Physical Chemistry C* **119,** 5152-5159 (2015).
18. Tas, G., & Maris, H. J. Picosecond ultrasonic study of phonon reflection from solid-liquid interfaces. *Physical Review B* **55,** 1852-1857 (1997).
19. Morath, C. J., & Maris, H. J. Phonon attenuation in amorphous solids studied by picosecond ultrasonics. *Physical Review B* **54,** 203 (1996).
20. Yilmaz, H., Pena-Francesch, A., Shreiner, R., Jung, H., Belay, Z., Demirel, M. C., Ozdemir, S. K., & Yang, L. Structural Protein-Based Whispering Gallery Mode Resonators. *ACS Photonics* **4,** 2179-2186 (2017).
21. Jung, H., Szwejkowski, C., Pena-Franchesh, A., Tomko, J. A., Allen, B., Ozdemir, S. K., Hopkins, P. E., & Demirel, M. C. Ultrafast Laser-Probing Spectroscopy for Studying Molecular Structure of Protein Aggregates. *Analyst* **142,** 1434-1441 (2017).
22. Sariola, V., Pena-Francesch, A., Jung, H., Cetinkaya, M., Pacheco, C., Sitti, M., & Demirel, M. C. Segmented molecular design of self-healing proteinaceous materials. *Scientific reports* **5,** 13482 (2015).
23. Pena-Francesch, A., Florez, S., Jung, H., Sebastian, A., Albert, I., Curtis, W., & Demirel, M. C. Materials Fabrication from Native and Recombinant Thermoplastic Squid Proteins. *Advanced Functional Materials* **24,** 7401-7409 (2014).
24. Hu, X., Kaplan, D., & Cebe, P. Effect of water on the thermal properties of silk fibroin. *Thermochimica Acta* **461,** 137-144 (2007).
25. Meyer, A., Dimeo, R. M., Gehring, P. M., & Neumann, D. A. The high-flux backscattering spectrometer at the NIST Center for Neutron Research. *Review of Scientific Instruments* **74,** 2759-2777 (2003).
26. Copley, J. R. D. & Cook, J. C. The Disk Chopper Spectrometer at NIST: a new instrument for quasielastic neutron scattering studies. *Chemical Physics* **292,** 477-485 (2003).

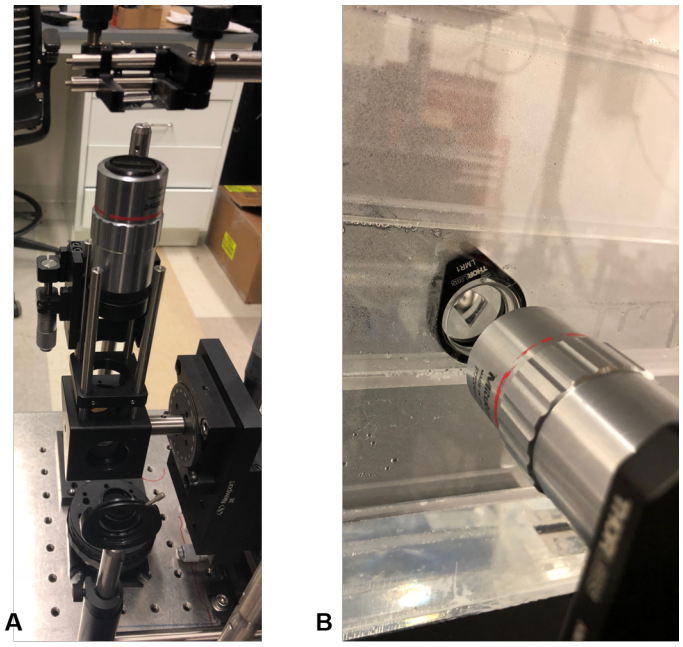

Supplementary Figure 1. a) Photograph of our beam/sample alignment for probing upwards, through the transparent substrate, of our samples; a calibration sample (SiO_2) is being above the objective. **b)** Photograph of our optical access window to the humidity chamber used. The chamber rests on a stage with 3-axis movement for back-alignment of the sample.

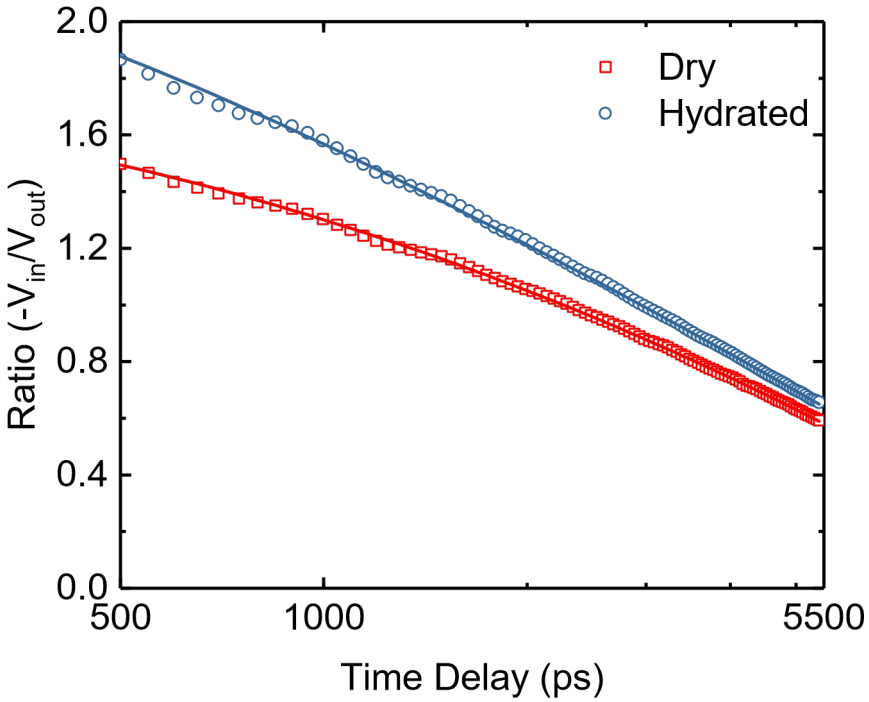

Supplementary Figure 2. The acquired ratio of V_{in}/V_{out} signals for TR-n25 in the ambient and hydrated case.

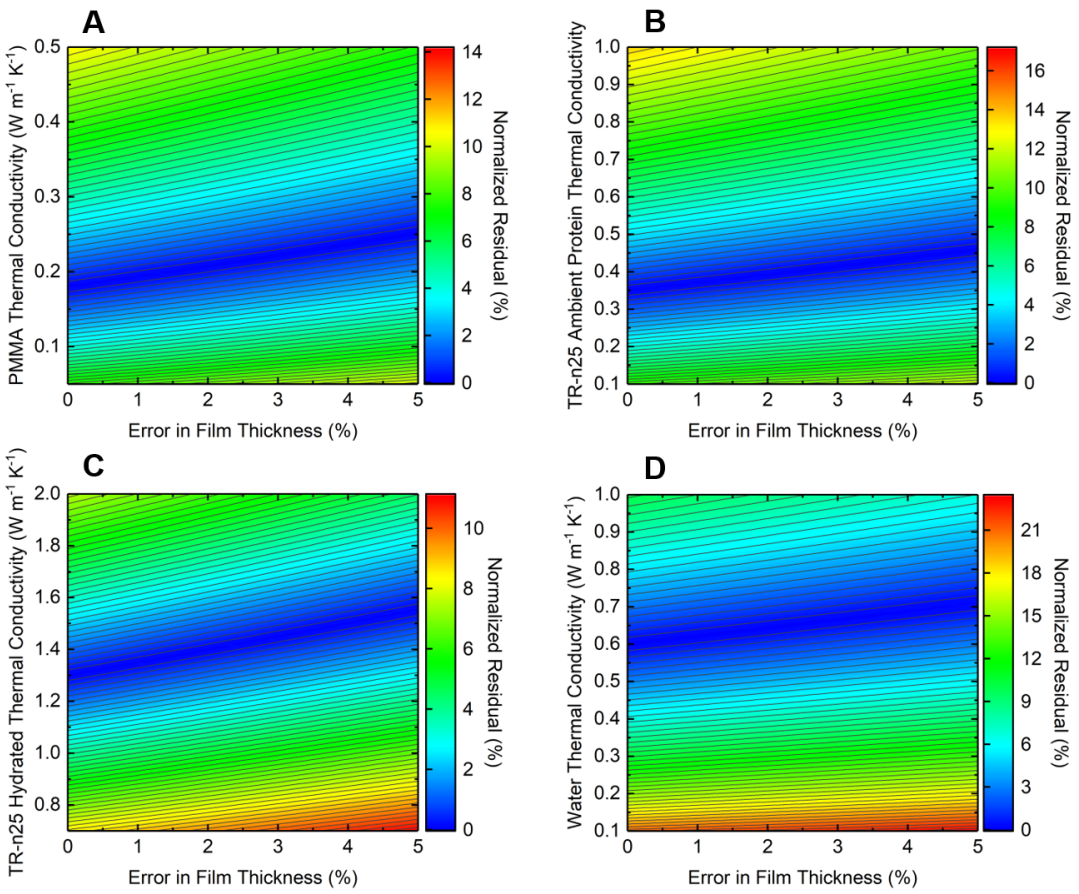

Supplementary Figure 3. The normalized residual (i.e., the accuracy of the models fit relative to the obtained thermal decay curve) for values of best-fit for our bi-directional thermal model for various media on 80 nm Al/SiO2 supports; the media are **a)** our TR films in an ambient state, **b)** hydrated TR-n25 (the largest thermal conductivity measured in this work), **c)** PMMA as a reference for the sensitivity of TDTR to low thermal conductivity films in a bidirectional experimental setup, and **d)** a drop of water.

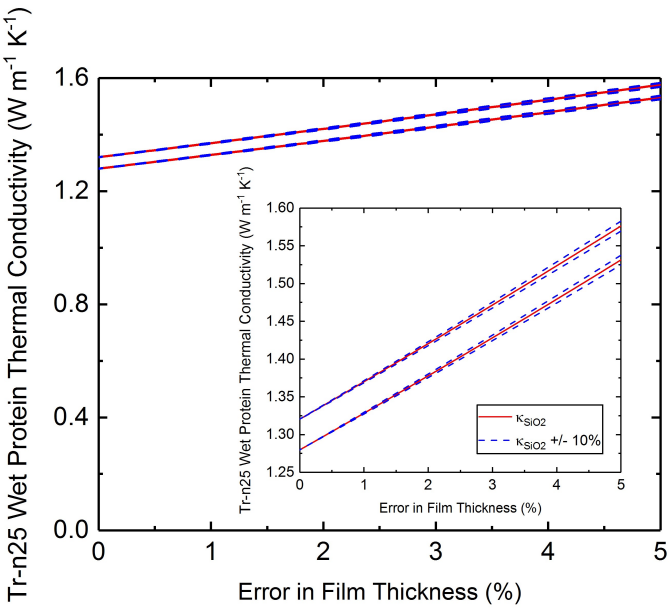

Supplementary Figure 4. The inner-most contour, or the model's best fit, as shown in Fig. S3, for thermal conductivity values of SiO_2 within 10% of the measured value (1.35 W m^{-1} K^{-1}). As seen, the thermal model is most sensitive to the thickness of the metal transducer.

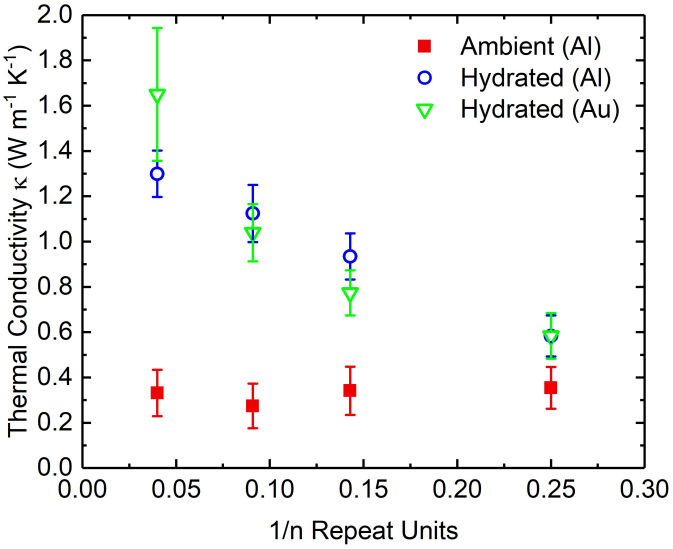

Supplementary Figure 5. Measured thermal conductivity as a function of inverse repeat units, 1/*n*, for both 80 nm Al and Au metal transducers.

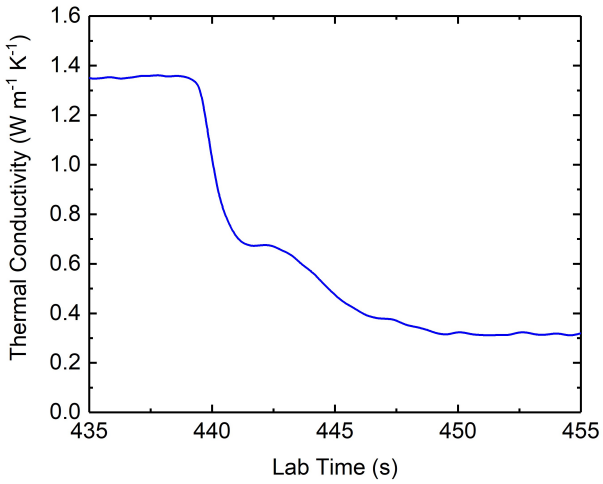

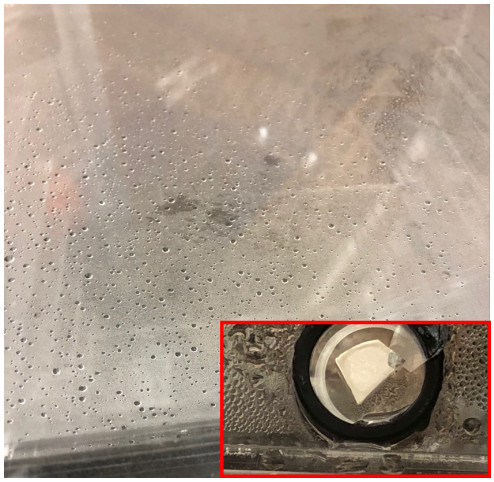

Supplementary Figure 6. a) A zoomed-in view of the measured thermal conductivity as a function of real time for TRn25, providing insight to the time-scale associated with switching from a hydrated to ambient state. Note, the ambient-to-hydrated switch is consistently within the time constant of our lock-in amplifier (300 ms), thus appearing instantaneous. **b)** Image of our humidity chamber at a relative humidity of approximately 85%. The inset shows a TR-n11 sample (supported by an 80 nm Al transducer and 1 mm SiO_2 substrate underneath) on the optical window inlet to the chamber. As seen, condensation occurs heavily throughout the chamber.

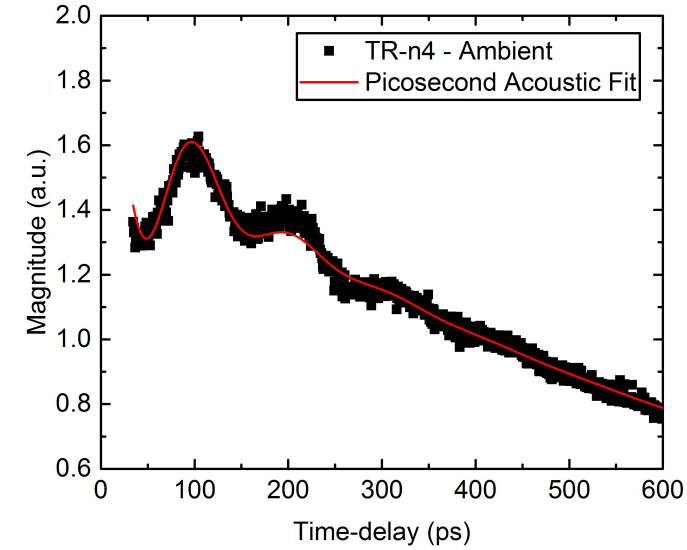

Model	Picosecond Acoustics
Equation	A*exp(-Gamma*x)*cos((2*pi*x /Period)-delta) - B*exp(-x/tau)
A	0.55684 ± 0.02469
Gamma	0.01457 ± 5.69043E-4
Period	108.72648 ± 1.111
tau	790.09421 ± 3.97826
B	-1.6844 ± 0.00338
delta	-50.47406 ± 0.05114
Reduced Chi-Sqr	8.44304E-4
R-Square(COD)	1
Adj. R-Square	1

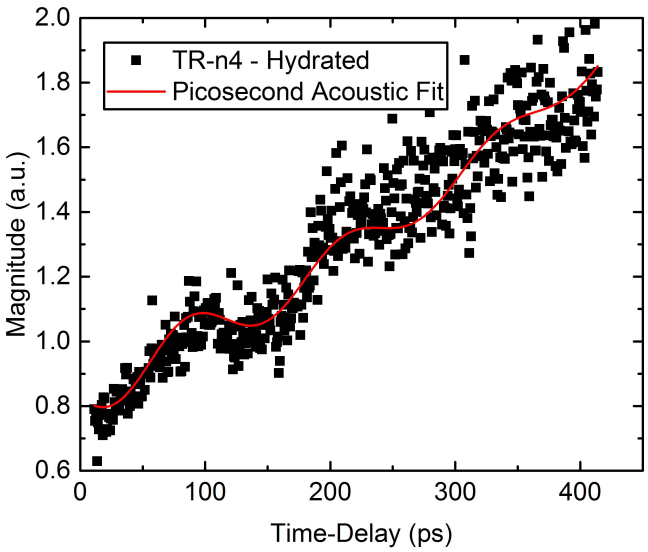

Model	Picosecond Acoustics
Equation	A*exp(-Gamma*x)*cos((2*pi*x /Period)-delta) - B*exp(-x/tau)
A	0.09217 ± 0.01516
Gamma	0.00226 ± 8.9156E-4
Period	123.64821 ± 2.39508
tau	-520.90579 ± 8.2342
B	-0.84695 ± 0.00726
delta	4.49517 ± 0.18772
Reduced Chi-Sqr	0.00938
R-Square(COD)	1
Adj. R-Square	1

Supplementary Figure 7. Examples of TDBS measurements on n-4 in the ambient **(top)** and hydrated states **(bottom)**, with values of best fit tabulated for each.

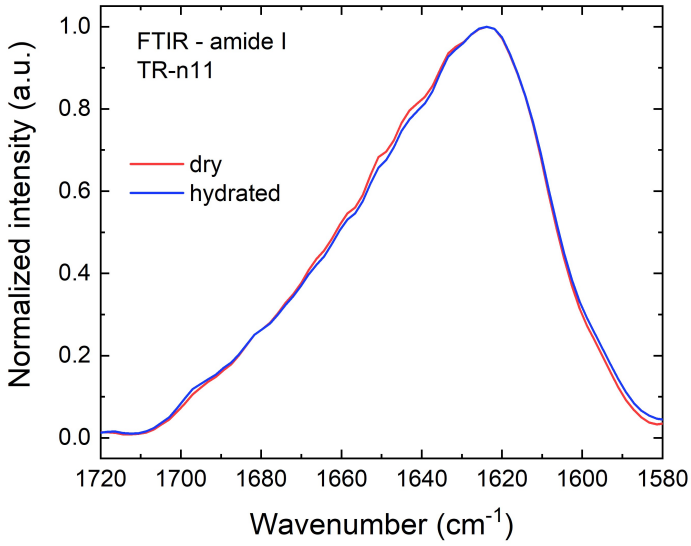

Supplementary Figure 8. FTIR amide I analysis of ambient and hydrated TR-n11 protein.

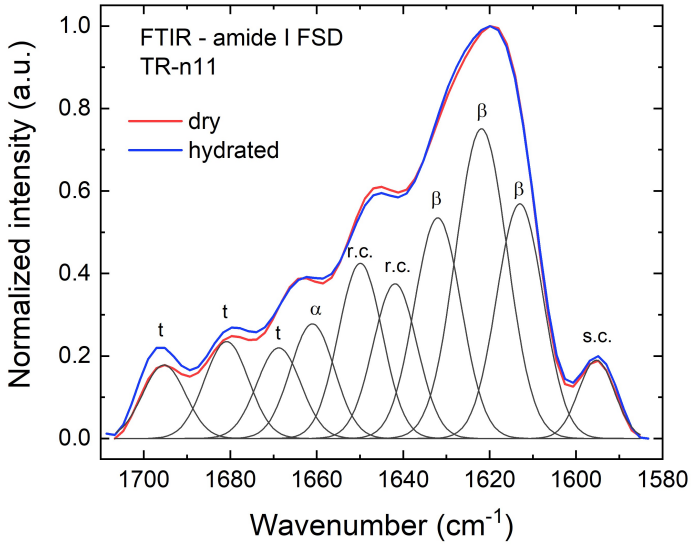

Supplementary Figure 9. FTIR amide I FSD analysis of ambient and hydrated TR-n11 protein.

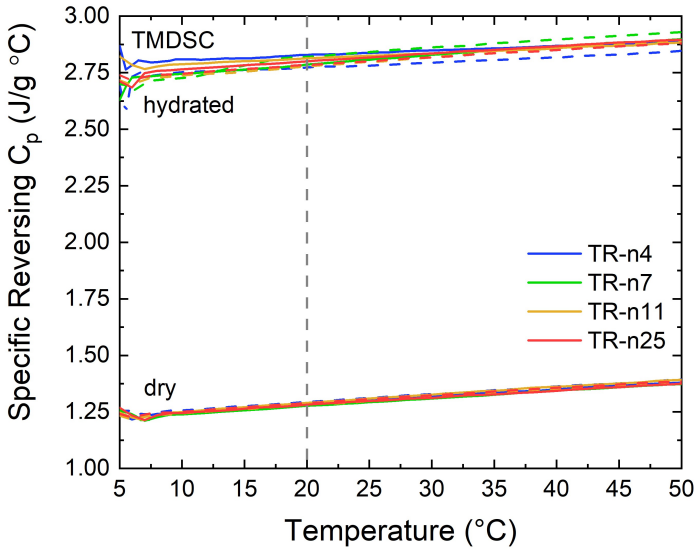

Supplementary Figure 10. Specific reversing C_p measurements on ambient and hydrated TR proteins by TMDSC. Two measurements (solid line for first measurement, dashed line for repetitions) per sample are plotted. Vertical line denoted the temperature of interest (20 °C) for the calculation of C_p.